ORIGINAL PAPER

Quantitative Analysis and 3D Visualization of Crack Behavior in 3D-Printed Rock-Like Specimens with Single Flaw Using In-Situ Micro-CT Imaging

Yulong Shao[1] · Jingwei Yang[2] · Jineon Kim[1] · Seyedahmad Mehrishal[1] · Jae-Joon Song[1]

Abstract

3D printing technology allows for precise control of preparing complex geometries and internal defects in printed rock analogs, while in-situ Micro-CT imaging enables real-time observation of crack behavior. The combination of these technologies offers a new research approach for studying rock crack behavior. In this study, 3D-printed rock-like specimens containing a pre-existing flaw were prepared using a gypsum powder-based 3D printer. An advanced in-situ Micro-CT system equipped with a loading device was used to quantitatively and visually investigate the crack behavior in 3D-printed specimens under uniaxial compression testing. 2D CT images obtained from in-situ compression testing at different deformations could be used to reconstruct a 3D model and visually identify the crack patterns of the extracted cracks in 3D-printed specimens. The initiation angle of cracks, volume of the pre-existing flaw, volume of newly formed cracks, and damage value with respect to strains were analyzed to quantitatively investigate crack behavior. The results indicated that within the 3D-printed specimens, tensile cracks were first initiated near the internal flaw, followed by the occurrence of shear cracks or tensile-shear mixed cracks at the flaw tips. Additionally, there was a negative linear correlation between the initiation angle of newly formed cracks and the initial flaw angle. For flaw angles in the range of $0° \leq \alpha \leq 45°$, a higher number of newly formed cracks were observed in the 3D-printed specimens, and the rates of increase in crack volume and damage values with strain were faster. However, for flaw angles in the range of $45° < \alpha \leq 90°$, the results showed the opposite trend. Furthermore, through comparison with the crack behavior of natural rocks containing a single flaw, it was found that the failure modes and crack behavior of the 3D-printed specimens exhibit certain similarities with natural rocks.

Highlights

- In-situ Micro-CT tests were performed on 3D-printed specimens with a single flaw during uniaxial compression.
- Crack behavior in 3D-printed rock-like specimens during uniaxial compression were visually and quantitatively investigated.
- Damage evolution of the initial flaw and newly formed cracks in 3D-printed rock-like specimens were respectively discussed.
- Comparison of crack behavior between 3D-printed specimens and natural rocks were investigated.

✉ Jae-Joon Song
  songjj@snu.ac.kr

1 Department of Energy Resources Engineering, Research Institute of Energy and Resources, Seoul National University, Seoul 08826, Republic of Korea

2 Department of Civil and Environmental Engineering, Seoul National University, 1 Gwanak-ro, Gwanak-gu, Seoul 08826, Republic of Korea

1 Introduction

Discontinuities are pervasive in natural rock masses, significantly influencing their deformation and cracking behavior (Sharafisafa et al. 2018). Understanding the mechanics and deformation-cracking behavior of discontinuities is consequently essential for various rock engineering applications such as the efficient extraction of geo-energy as well as the long-term safety of underground engineering projects (He et al. 2021; Pardoen et al. 2020; Song et al. 2022, 2023a). The mechanical properties and fracture behavior of natural rocks with preliminary defects, including those of sandstone (Xu et al. 2021a; Yang et al. 2013), shale (Ban et al. 2022; Li et al. 2021), granite (Yang and Huang 2017; Yin et al. 2014), limestone (Dewanckele et al. 2013; Feng et al. 2009), and marble (Li et al. 2005; Zou and Wong 2014), have been extensively investigated as well as rock-like specimens with pre-existing flaws (Cao et al. 2015; Wang et al. 2019; Wong et al. 2001). In the above studies, the mechanical properties and the deformation-cracking responses of rock samples were mainly studied in relation to the number of prefabricated fractures (Cao et al. 2015; Dewanckele et al. 2013; Feng et al. 2009; Li et al. 2005; Wang et al. 2019; Wong et al. 2001) and their morphology (Ban et al. 2022; Li et al. 2021; Xu et al. 2021a; Yang and Huang 2017; Yang et al. 2013; Yin et al. 2014; Zou and Wong 2014). The results confirmed that the presence of initial fractures reduced the mechanical strength of rock specimens, and the extent of weakening was influenced by the geometrical parameters of the fractures. However, it is challenging to prepare rock specimens with flaws because traditional methods are limited, not cost-effective, and error-prone, such as water jet cutting, molding, and ultrasonic machining (Yang et al. 2017).

The advantages of 3D printing technology include precise fabrication, flexibility, high repeatability, and the ability to prepare complex geometries and internal defects, which have attracted significant attention in the rock mechanics field (Sharafisafa et al. 2018). Some researchers have conducted studies comparing the mechanical properties and failure modes of 3D-printed intact specimens using different printing materials, such as PLA (polylactic acid) (Jiang and Zhao 2015; Jiang et al. 2016b), resin (Gao et al. 2021; Zhou and Zhu 2018), gypsum (Shao et al. 2023a, b; Wu et al. 2020), sand (Niu et al. 2023; Xu et al. 2021b), and cement (Feng et al. 2019; Mei et al. 2022), with those of natural rocks. They aimed to explore the potential of printing materials to be used as substitutes for natural rocks. Other researchers (Jiang et al. 2016a; Tian and Han 2017; Yang and Huang 2017; Zhu et al. 2018) have focused on studying the deformation and crack propagation of 3D-printed specimens under loading. They utilize the capabilities of 3D printing technology to precisely construct crack structures with varying shapes, sizes, and complexities inside the specimens, addressing the challenge of creating such precise crack geometries in conventional rock mechanics testing. Zhou et al. (2019; 2020) performed static and dynamic laboratory tests on 3D-printed resin specimens with 3D embedded flaws to study the volumetric fracturing and mechanical properties. The results indicated that flaw geometry has a remarkable influence on the mechanical and fracture behaviors of the flawed samples. Sharafisafa et al. (2018) manufactured 3D-printed Brazilian disc specimens with pre-existing single and double flaws using gypsum material to investigate the loading capacity as well as the crack initiation, propagation and coalescence mechanism of pre-flawed rock-like specimens. The results showed that the 3D-printed gypsum specimens not only can produce mechanical properties that are similar to natural brittle rock but also has advantages such as material homogeneity, high geometry flexibility, easy pre-flaw implementation and quickness in prototyping. Tian and Han (2017) prepared 3D-printed sand specimens and conducted a series of mechanical experiments to investigate the influence of number and inclination angle of pre-existing flaws on strength and failure patterns under uniaxial compression, which indicated that 3DP specimens had similar mechanical properties with rock-type materials. However, the aforementioned studies on crack behavior in 3D-printed specimens are primarily based on surface observations, which limits the comprehensive understanding of crack initiation and propagation processes. Furthermore, it is difficult to quantitatively assess the damage progression and to elucidate the crack growth mechanisms and fracture behavior through surface observations.

In recent years, the combination of 3D printing technology with high-resolution CT imaging has become a prominent research approach in rock mechanics. This trend is mainly driven by the capability of CT imaging to investigate microstructures within 3D-printed specimens, including pores and cracks (Feng et al. 2019; Kong et al. 2018). Additionally, CT scanning can be employed to obtain high-precision digital core data of natural rocks, which serves as input for 3D printing rock-like models with certain defects that resemble the internal features of natural fractures or joints (Yin et al. 2020; Zhu et al. 2018). Kong et al. (2018) characterized the pores properties of 3D-printed specimens by Micro-CT imaging and first proposed that 3D-printed rocks are vertically transversely isotropic. Ishutov et al. (2015; 2017; 2021) conducted multiple experiments on 3D-printed replications of pore networks obtained from CT scanning data of sandstone. The results denoted that accurate replication of pore networks depends on the resolution of tomographic images, rock specimen size, statistical algorithms for digital modeling, and the

resolution of 3D printing. Shao et al. (2023a, b) investigated microstructure properties, macroscopic mechanical behavior and failure modes of 3D-printed rocks based on the combined application of 3D printing and Micro-CT technologies, and indicated that the macroscopic mechanical behavior and failure modes of 3D-printed gypsum rocks are affected by the movement direction of the printer head and bedding plane. Zhu et al. (2018) proposed two methods, i.e., 3D printing and 3D numerical modeling, to replicate internal defects and study the mechanical and fracture behaviors of rock in combination with Micro-CT imaging technology. The results showed that both the 3D-printed specimens and the 3D numerical models can successfully replicate the internal defects and micro-structures of natural volcanic rock. Wu et al. (2022) investigated the effect of the internal pore and the fracture structure on the size effect of physical rock models using CT scanning and 3D printing techniques and effectively resolved the size effect in the mechanical behavior of natural rocks.

The integration of 3D printing technology with in-situ CT scanning has created a novel experimental approach, enabling the rapid fabrication of rock-like specimens and the simulation of their complex internal structures. Moreover, by combining real-time monitoring and quantitative analysis capabilities, it allows for the immediate observation of internal changes during loading, including the initiation and propagation of newly formed cracks. This method provides a deeper understanding and support for the study of rock mechanics properties and engineering applications, promising significant advancements in the field of rock research. While it is crucial to understand the micro-mechanism of crack propagation in 3D-printed specimens during loading, few studies have examined fracture behavior in 3D-printed specimens using the combination of 3D printing technology and in-situ CT technology. Mandal and Basu (2018) performed compression tests on 3D-printed scaffolds coupled with Micro-CT scanning and revealed that the layered microstructure is the main cause of failure. Liu et al. (2021) investigated the fracture evolution of 3D-printed gypsum specimens during loading using the in-situ Micro-CT system and employed fractal analysis to quantify the cracking process. The analysis results showed that the fractal dimension increases with the propagation of cracks. Song et al. (2023b) manufactured three types of intact 3D-printed specimens with silica sand and gypsum material to investigate the deforming-cracking process during UCS tests of the 3D-printed specimens using in-situ Micro-CT scanning. The results indicated that the failure of the 3D-printed specimen started from weak points of material cementation. However, to the authors' knowledge, there has been no prior investigation into the fracture behavior of 3D-printed specimens with a single flaw under compression tests utilizing an in-situ Micro-CT system.

In summary, a combination of in-situ CT imaging and 3D printing enables precise control in the manufacture of rock-like specimens with internal defects resembling natural fractures and joints, as well as the quantitative evaluation and visual observation of crack behavior during uniaxial compression experiments on 3D-printed specimens. This study aims to quantitatively and visually analyze the crack behavior of 3D-printed specimens with a single flaw using an advanced in-situ Micro-CT system equipped with a loading device. 3D-printed rock-like specimens containing a single flaw were manufactured by a gypsum powder-based printer. Leveraging high-resolution micro-CT imaging, we can dynamically observe and analyze crack propagation and interaction in real-time, capturing the intricate details of crack development within the 3D-printed specimens. The findings deepen our understanding of crack propagation in natural rock formations, shedding light on essential aspects of rock mechanics and geotechnical processes. This knowledge contributes to improved predictions of how cracks develop and initiate within a natural rock, crucial for assessing stability in engineering projects and geological hazard management.

2 Experiments and Methodology

2.1 Experimental Scheme

Figure 1 illustrates the experimental scheme of this study, which consists of the preparation of 3D-printed rock-like specimens, in-situ compression testing, 3D reconstruction, and extraction of cracks. The 3D-printed rock-like specimens were fabricated using a powder-based ZP450 printer (Fig. 1a), with ZP150 gypsum powder and Zb63 binder as the printing materials. Seven 3D-printed specimens with different inclined angles of single flaw ranging from 0° to 90° at 15° intervals were produced, as shown in Fig. 1b. Subsequently, these specimens underwent a 14-day heating treatment at 40 °C in an oven before conducting the compression experiments using the in-situ Micro-CT system, consisting of a Skyscan 1272 Micro-CT and loading device, as depicted in Fig. 1d. Numerous 2D CT images were obtained from in-situ compression tests at different deformations, as shown in Fig. 1e. The 2D CT images were then used to reconstruct a 3D model of the 3D-printed specimens, followed by crack extraction using Avizo software for further crack analysis. The steps of 3D reconstruction and crack analysis are depicted in Fig. 1f and g, respectively.
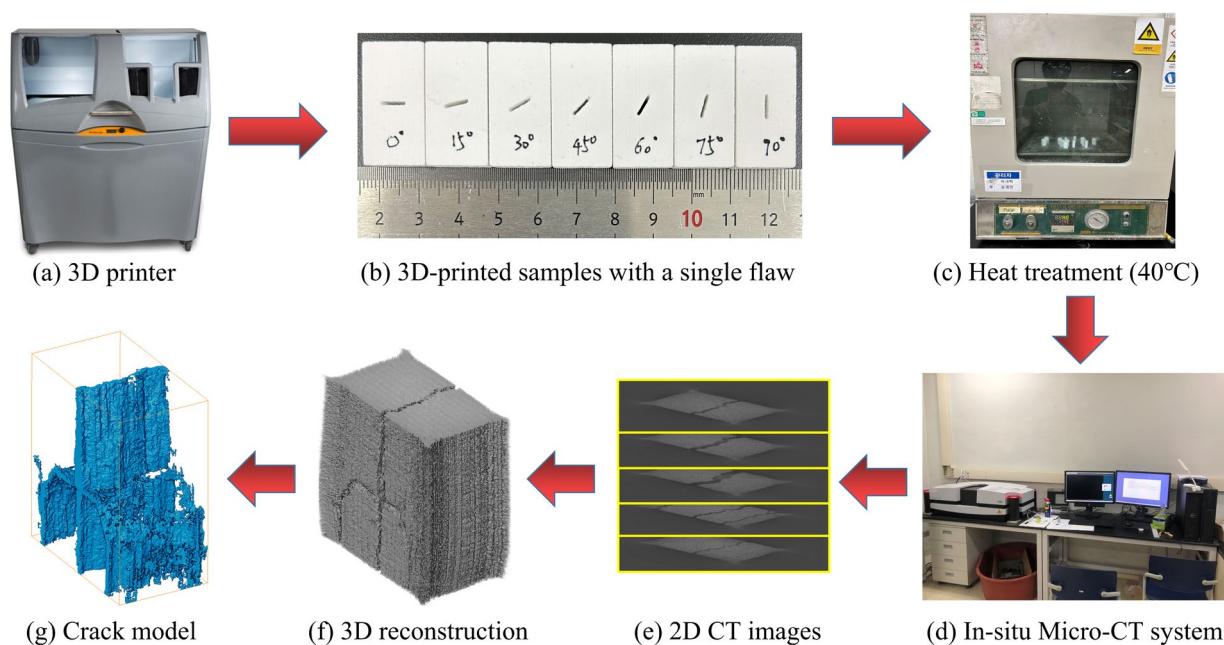
(a) 3D printer   (b) 3D-printed samples with a single flaw   (c) Heat treatment (40℃)

(g) Crack model   (f) 3D reconstruction   (e) 2D CT images   (d) In-situ Micro-CT system

Fig. 1 Experimental scheme of this study. The ZP450 printer from 3D Systems Corporation is used to fabricate 3D-printed specimens with ZP150 gypsum powder and Zb63 binder. The in-situ micro-CT system consists of the Skyscan 1272 Micro-CT and a loading device, which is capable of applying a maximum compressive force of 5kN

2.2 Size of the Specimen and Initial Flaw

The printing direction in 3D-printing yields significant variances in the physical performance of 3D-printed specimens across different directions, resulting in anisotropic characteristics (Fereshtenejad and Song 2016; Shao et al. 2023a, b). To eliminate the influence of layers on the mechanical properties, all 3D-printed specimens were fabricated along the z-axis direction, with the layers oriented perpendicular to the printing direction, as illustrated in Fig. 2a. The loading device used in the in-situ compression tests imposes certain limitations on the sample dimensions, requiring a sample diameter not exceeding 22 mm. Therefore, 3D-printed specimens were fabricated as cuboids measuring 30 mm in height, 15 mm in length, and 9 mm in width, taking into account the size limitation of the in-situ Micro-CT system. A pre-existing flaw with aperture of 1 mm and length of 6 mm was placed in the center of the 3D-printed specimen, as depicted in Fig. 2b. To investigate the influence of crack inclination angle on the crack behavior of 3D-printed specimens, seven specimens with different inclination angles ranging from 0° to 90° were prepared, as shown in Fig. 2c.

2.3 In-Situ Micro-CT System and Scanning Steps

Figure 3a illustrates the in-situ Micro-CT uniaxial compression system, which comprises three main components: the X-ray source, the detachable loading apparatus, and the detector. A commercial Skyscan Material Testing Stage (MTS), the loading apparatus, is installed inside a Skyscan 1272 Micro-CT scanner to compose the in-situ Micro-CT uniaxial compression system. The working principle of the in-situ Micro-CT uniaxial compression system is shown in Fig. 3b. X-rays are generated from the X-ray source and transmitted through the sample. The transmitted X-rays are then recorded by the X-ray detector as a 2D projection image. The sample is incrementally rotated on the rotational stage while acquiring 2D projection images at each rotation angle. This process is repeated over a full 360° rotation, generating a series of 2D cross-sectional images that are subsequently reconstructed into a 3D model using computational techniques. The in-situ Micro-CT compression system operates in two scanning modes: (1) displacement-controlled scanning and (2) force-controlled scanning. In the displacement-controlled mode, Micro-CT images are scanned when the loader reaches predetermined displacements, at which the displacement is kept constant during scanning, as illustrated in Fig. 4a. In the force-controlled scanning mode, the specimens are scanned at predetermined forces with the force kept constant during scanning, as shown in Fig. 4b.

To investigate the crack behavior of 3D-printed specimens at different stages, this study employed the displacement-controlled scanning mode, controlling the Micro-CT operations by predetermined displacements. The
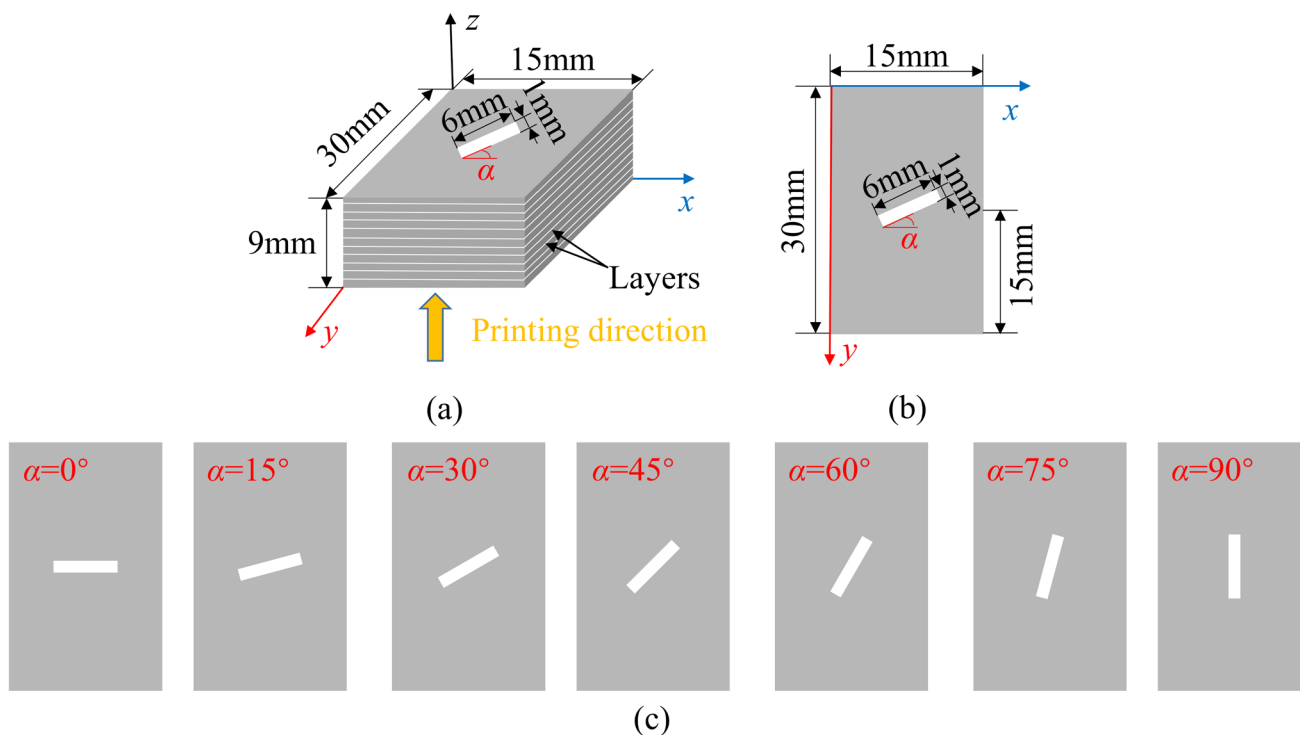
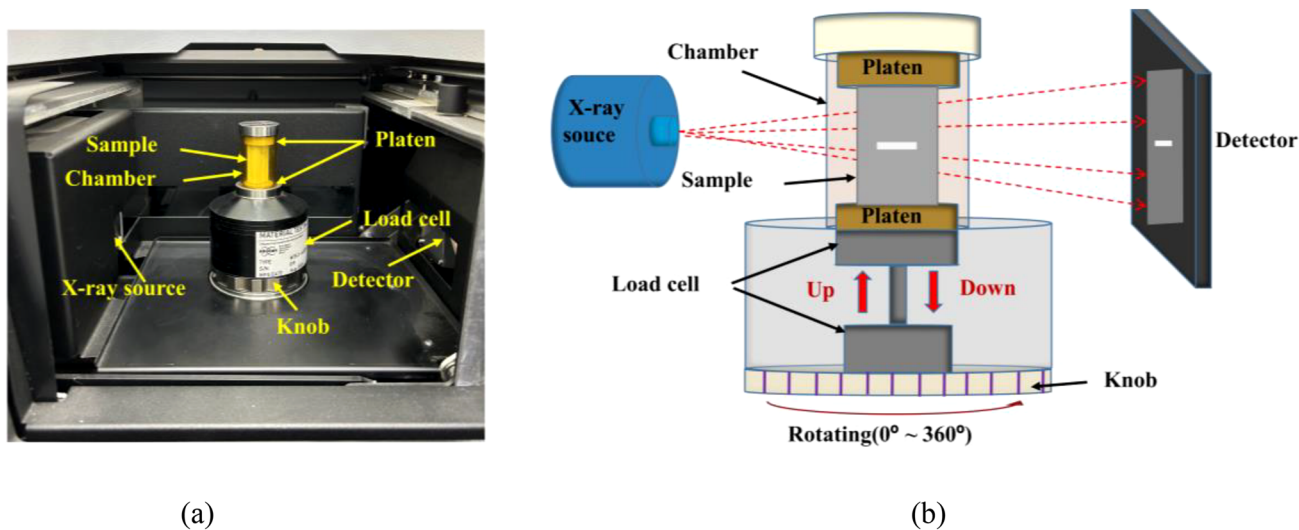**Fig. 2** Printing scheme (**a**) and 3D-printed specimens with initial flaw (**b**)

Fig. 3 In-situ Micro-CT uniaxial compression system (**a**) and schematic diagram (**b**)

image resolution obtained from CT scanning was 20.9 µm and the loading rate was 4 µm/s for all compression tests. The stress–strain curves of compression tests of 3D-printed specimens with single flaws of different incline angles are shown in Fig. 5, with blue dots indicating the CT scanning steps. In this study, the selection of scanning steps was carefully considered for several reasons. First, to address the limitations of CT scanning in terms of maximum scan duration and precision during in-situ compression tests, we opted to limit the number of scans per sample to six to avoid potential equipment damage and decreased image accuracy. Second, unlike previous studies, our focus was on monitoring the evolution of the initial flaw and the appearance of newly formed cracks with increasing strain.
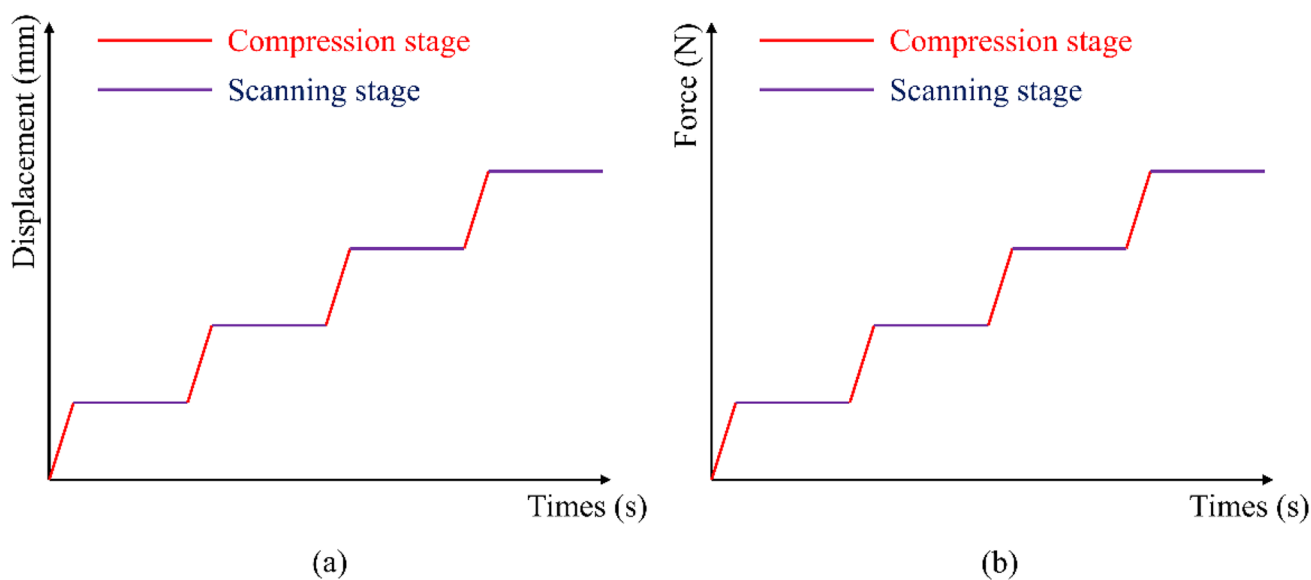
Fig. 4 Displacement-controlled scanning mode (**a**) and force-controlled scanning mode (**b**)

Thus, the scanning steps were distributed across various stages of the stress–strain curve for each 3D-printed gypsum specimen, namely, the stages of crack initiation, propagation, and eventual failure, to effectively capture the crack behavior during the uniaxial compression test. It is worth noting that during the process of in-situ compression tests, noticeable stress drops are observed at each scanning step. This is mainly because the loading apparatus stops moving to maintain constant displacement and initiates scanning for imaging at each scan. However, due to the relatively long time required for scanning (approximately 3 h), coupled with the low strength of the 3D-printed gypsum specimens, significant stress relaxation inevitably occurs. Similar phenomena have been reported in previous studies (Duan et al. 2022). To address or alleviate the issue of stress drops, several methods can be taken, such as improving the strength of the 3D-printed gypsum specimens or reducing the CT scanning time. This will be one of the key focuses for future research endeavors. The stress and strain values corresponding to the scanning steps of each 3D-printed specimen are tabulated in Table 1.

2.4 Selection of the Analysis Region

The height of the region of the specimen scanned by Micro-CT was limited to 17 mm, due to the limitation in scanning range when scanning with a resolution of 20.9 μm. The scanned region of the 3D-printed specimen is indicated by the yellow area in Fig. 6a, with the dimensions of 17 mm in height, 15 mm in length, and 9 mm in width, as depicted in Fig. 6b. During the CT scanning process, the region near the surface of the 3D-printed specimen is often directly exposed to air, which can lead to pseudo-shadow effects in the images caused by X-ray diffraction and scattering at the specimen's surface (Kang et al. 2022). This may result in boundary-blurring or overlapping in the CT images, potentially affecting the CT image quality. To mitigate this, a slightly smaller region is typically selected for further 3D reconstruction and microstructural analysis. In this study, the analysis region for crack extraction was selected with dimensions of 17 mm in height, 14.9 mm in length, and 8.5 mm in width, as shown in Fig. 6c.

3 Results and Analysis

3.1 Visual Analysis of Crack Behavior

A number of classification methods have been employed to describe crack patterns observed during experiments or numerical studies to characterize cracks that originate from a pre-existing flaw (Miao et al. 2018). For instance, based on the crack morphology, cracks can be categorized into wing cracks and anti-wing cracks (Dyskin et al. 1994, 2003; Liang et al. 2012); based on the timing of crack initiation, cracks can be classified as primary cracks and secondary cracks (Aliabadian et al. 2021; Wang et al. 2021; Zhou et al. 2015). However, these crack classification methods were limited to cracks that occur before rock failure. To address this limitation, Wong and Einstein (2009) introduced a practical crack characterization scheme that can describe different crack trajectories and initiation mechanisms simultaneously. Figure 7 illustrates the crack pattern classification used in
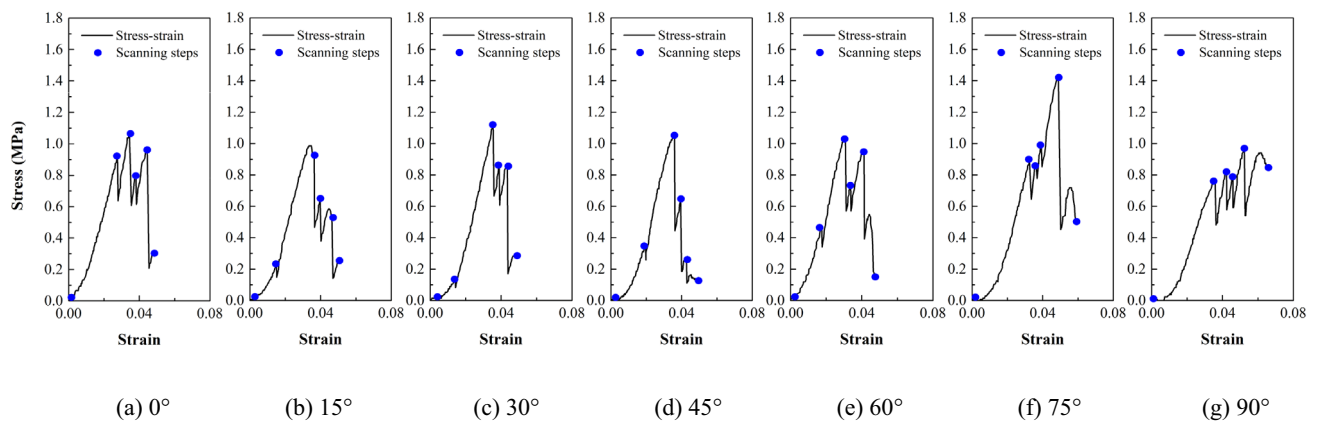
Fig. 5 Stress–strain curves of 3D-printed specimens with different incline angles of single flaw subjected to in-situ compression tests. Blue dotes indicate the scanning steps of each test

Table 1 Strain and stress values at different scanning steps of 3D-printed specimens with different incline angles of a single flaw

Inclined angle (α)	First scanning		Second scanning		Third scanning		Forth scanning		Fifth scanning		Sixth scanning	
	Strain	Stress (MPa)	Strain	Stress (MPa)	Strain	Stress (MPa)	Strain	Stress (MPa)	Strain	Stress (MPa)	Strain	Stress (MPa)
0°	0.0015	0.0167	0.0276	0.9129	0.0344	1.0586	0.0381 (*)	0.799	0.0445 (*)	0.9581	0.0476 (*)	0.3033
15°	0.0025	0.0238	0.0151	0.2286	0.0364 (*)	0.9238	0.0397 (*)	0.6429	0.0464 (*)	0.5243	0.0503 (*)	0.2519
30°	0.006	0.0248	0.0141	0.1343	0.0355	1.1214	0.0389 (*)	0.8562	0.0435 (*)	0.8459	0.049 (*)	0.2919
45°	0.0023	0.0157	0.0196	0.3448	0.036	1.0529	0.0395 (*)	0.6414	0.0427 (*)	0.2624	0.0495 (*)	0.1276
60°	0.0018	0.0252	0.0176	0.4686	0.0308	1.0323	0.0338 (*)	0.7276	0.0413 (*)	0.9491	0.0472 (*)	0.1557
75°	0	0	0.0324	0.8938	0.0363	0.8591	0.0392	0.9871	0.0489	1.4238	0.059 (*)	0.5028
90°	0	0	0.0358	0.7619	0.0423	0.8238	0.0459	0.7867	0.0523	0.9629	0.0653 (*)	0.8524

The asterisk (*) denotes scanning steps after specimen failure

this study, where T1, T2, T3, M, S1, S2, and S3 represent cracks that initiate from the flaw tips as defined by Wong and Einstein (2009), and T4 denote cracks that initiate from the middle of the flaw, which is a classification newly introduced in this study. Type 1 tensile cracks (T1) are the initial wing-shaped cracks that start near the two flaw tips and propagate towards the axial stress location in a stable manner throughout the loading process. Their initiation position is influenced by the inclined angle of the pre-existing flaw. Tensile cracks of type 2 (T2) first develop along flaws and then move vertically towards the applied load. Type 3 tensile cracks (T3) display an anti-wing appearance, typically initiating during the post-peak stage with smooth surfaces which do not contain pulverized or broken materials. Type 4 tensile cracks (T4) initiate at the middle section of a pre-existing flaw, generally when the pre-existing crack angle is small, and once present, they are the first to be activated and propagate along the loading direction during uniaxial compression experiments. Despite the similar appearance of type 1 shear cracks (S1) and type 2 tensile cracks (T2),

the crack patterns are different in terms of displacement. The propagation direction of type 2 shear cracks (S2) is coplanar or quasi-coplanar to the flaw itself. Similarly, shear cracks of type 3 (S3) resemble tensile cracks of type 3 (T3), but they are distinct in terms of their displacement direction. The mixed tensile-shear cracks (M) comprise both tensile and shear displacement.

3.1.1 Crack Behavior in 2D

Figure 8 shows the 2D CT projection images of 3D-printed specimens containing a single flaw with different inclined angles obtained at different scanning steps. The crack evolution during the uniaxial compression test of 3D-printed specimens was qualitatively described by adopting the crack classification defined in Fig. 7. The time sequence of crack initiation was numbered by 1, 2, and 3; For example, T2_1 indicates the tensile crack of T2 type that forms the earliest, while S2_2 indicates a shear crack that forms shortly after the primary crack. We observed a notable similarity between the crack types and crack morphologies

Fig. 6 Schematic diagram of position of scanning region (**a**), dimension of scanning region (**b**), and dimension of the analysis region (**c**)
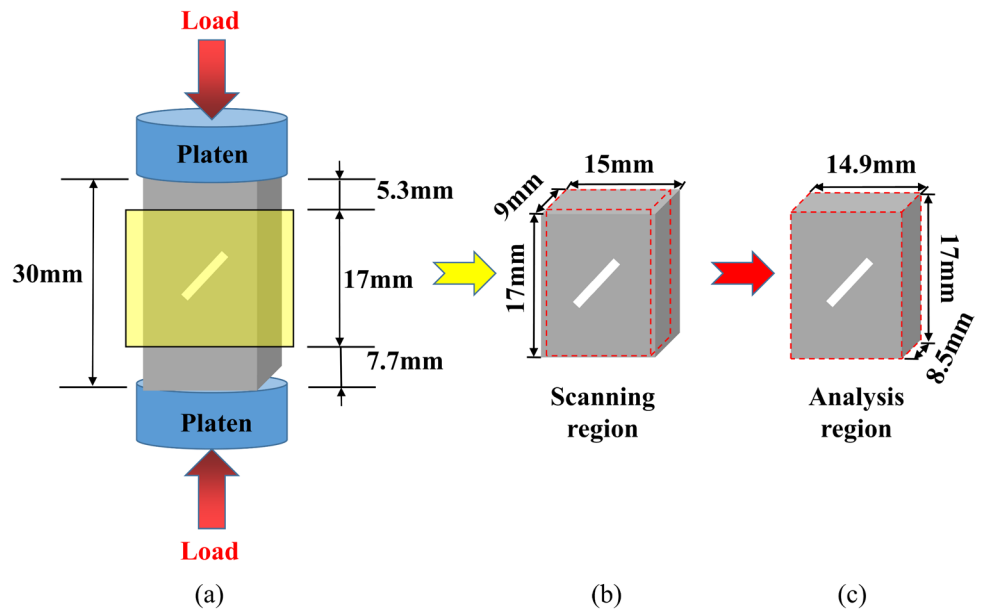

Fig. 7 Crack pattern classification used in this study, where T1, T2, T3, M, S1, S2, and S3 defined by Wong and Einstein (2009)

in the 3D-printed specimens with those previously reported in naturally fractured rocks (Li et al. 2021; Miao et al. 2018). Specifically, for pre-existing flaws with inclined angles within the range of $0° \leq \alpha \leq 30°$, the T4-type tensile cracks were initially generated at the middle of the flaw, followed by S1-type shear cracks or mixed-mode cracks (M) that initiated at both flaw tips. For flaw angles of $\alpha = 45°$

or $\alpha = 60°$, the primary cracks were T1 or T2-type tensile cracks, which were accompanied by S2-type shear cracks at the ends of the flaw. For the specimen with a flaw angle of $\alpha = 75°$, both T2-type tensile cracks and S2-type shear cracks were simultaneously initiated as primary cracks, followed by the generation of additional S2-type shear cracks at the lower end of the crack. At a flaw angle of $\alpha = 90°$, co-planar
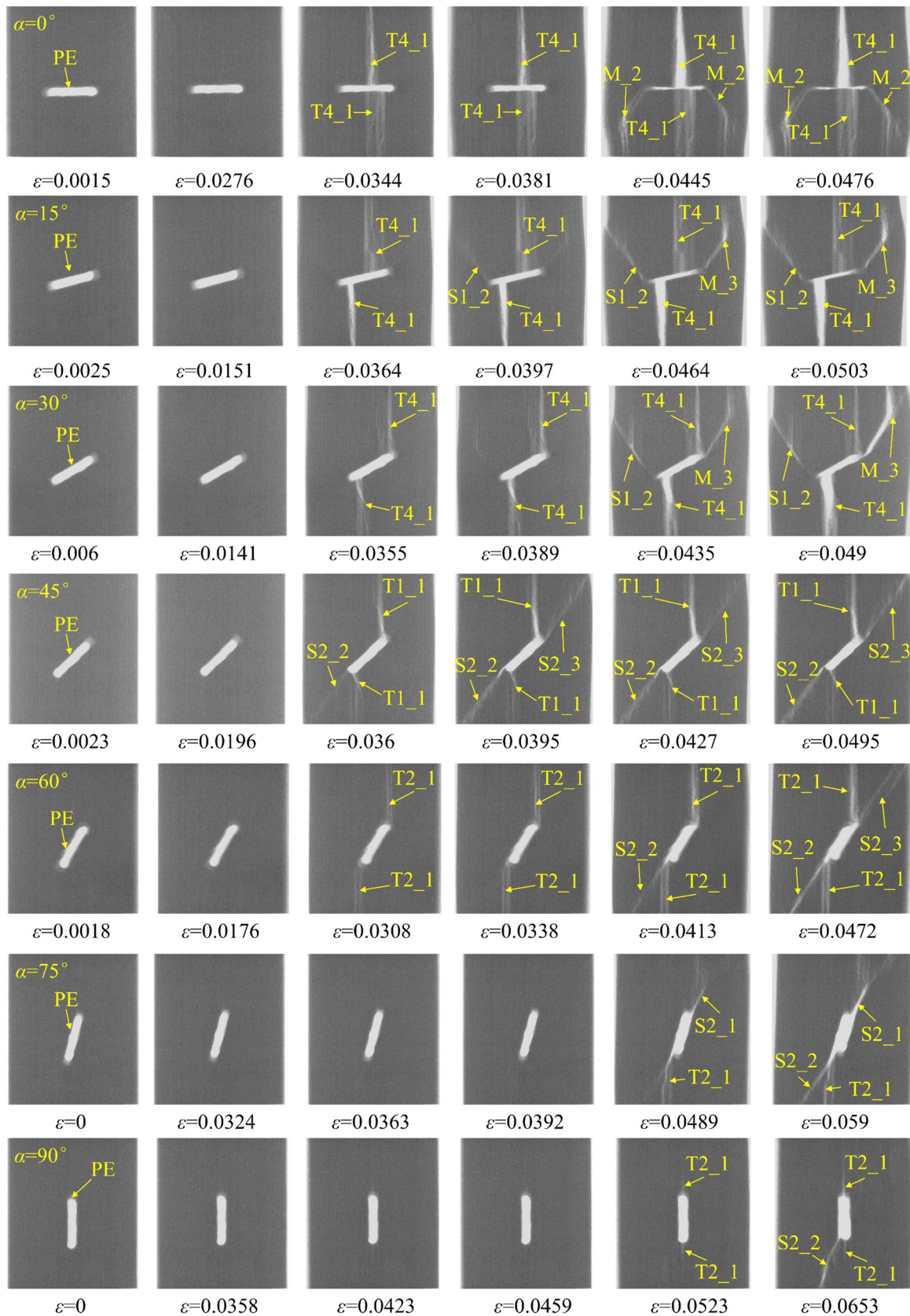
Fig. 8 Crack evolution of 3D-printed specimens containing a single flaw with different inclined angles at different scanning steps: 2D visualization. The crack classification referred to in this figure is detailed in the text. PE denotes the pre-existing flaw
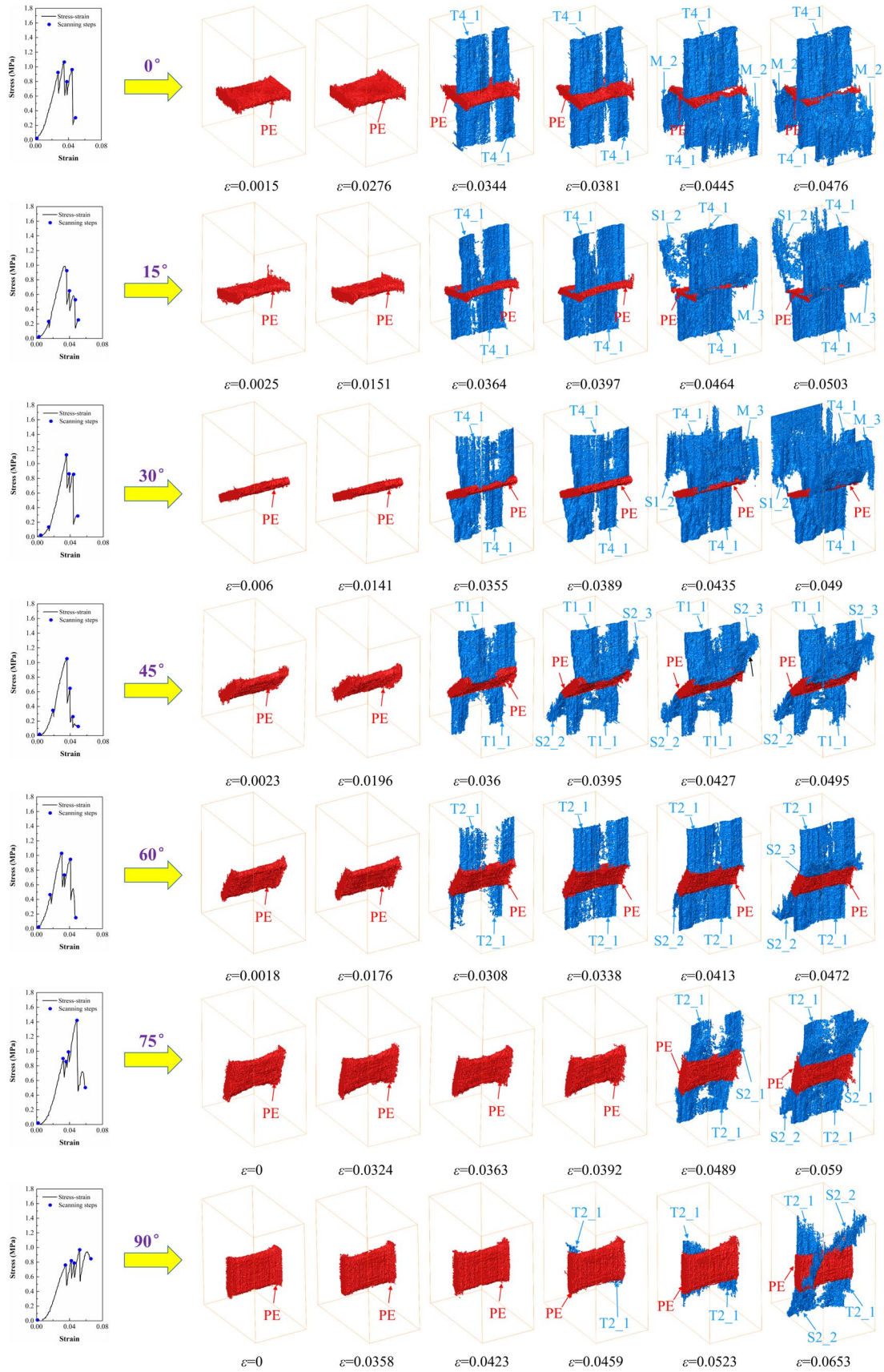
Fig. 9 Crack evolution of 3D-printed specimens containing a single flaw with different inclined angles at different scanning steps: 3D visualization. The pre-existing flaw is indicated in red and the cracks newly formed during compression are indicated in blue

T2-type tensile cracks were initiated at both ends of the crack, leading to the subsequent occurrence of S2-type shear cracks at the lower flaw tip. We also observed that with an increase in flaw angle, the initiation locations of primary cracks gradually shift from the middle to the end of flaw tips. Specifically, the primary T4-type tensile cracks transformed into T1 or T2-type tensile cracks as the flaw angle increased. The corresponding strain value at failure also increased, indicating a diminishing effect of tensile cracks at failure.

3.1.2 Crack Behavior in 3D

The obtained 2D CT images were reconstructed into 3D models to visualize the crack propagation during uniaxial compression experiments in 3D. The internal cracks were extracted and the crack morphologies at different scanning stages were investigated, as shown in Fig. 9. According to Figs. 8 and 9, while crack propagation patterns in 3D-printed specimens were generally consistent between 2 and 3D views, some crack information was omitted in the 2D view due to the absence of an additional dimension. For instance, for the specimen with flaw angle of $\alpha = 90°$, the strain value corresponding to the initiation of T2-type tensile cracks differed between the 2D view (0.0523) and the 3D view (0.0459). Moreover, the number and distribution of S2-type shear cracks showed inconsistencies, as S2-type shear cracks appeared only at the lower end of the pre-existing crack in the 2D view, while the 3D view revealed that they formed at both ends of the pre-existing crack. Referring to the stress–strain values of each scanning step (Table 1), cracks in 3D-printed specimens mostly occurred before peak stress (plastic deformation region) and rapidly developed after failure to form cracks that penetrated the specimens. This cracking behavior is consistent with the crack propagation patterns observed in naturally fractured rocks during uniaxial compression tests (Schultz 2019; Tutluoğlu et al. 2015). Furthermore, it is worth noting that the volume of the pre-existing flaw followed a certain trend during loading. For flaw angles within the range of $0° \leq \alpha \leq 45°$, the volume of the initial flaw decreased as the applied axial strain increased. However, when the flaw angle fell between $45° < \alpha \leq 90°$, the volume of the initial flaw either remained constant or increased. This finding is further discussed in the quantitative analysis in Sect. 3.2.

3.2 Quantitative Analysis of Crack Behavior

In comparison to traditional uniaxial compression tests, this study implemented an in-situ micro-CT uniaxial compression test which is capable of quantifying the crack behavior of 3D-printed specimens with a single flaw by reconstructing 3D images at different scanning stages. In this way, the crack evolution within the 3D-printed specimen could be accurately evaluated. The purpose of this section is to examine the crack initiation and propagation behavior of 3D-printed specimens with a single flaw from three perspectives: crack initiation angle, volume change of the initial flaw, and volume change of newly formed cracks.

3.2.1 Crack Initiation Angle

Identifying crack initiation mechanisms is essential for guiding crack propagation, evaluating fracture toughness, and analyzing flaws and stress distribution, which provide valuable insight into rock failure behavior and play a crucial role in the design of materials and structural safety assessment (Zhou et al. 2021). In this study, the crack initiation angle was defined as the acute angle between the line tangent to the propagation direction of newly formed cracks and the direction of the pre-existing flaw, as depicted in Fig. 10a. Table 2 summarizes the specifications of newly formed cracks, which include the crack type and their initiation angle. We compared the relationship between the initiation angle and the flaw angle among different natural rocks (Sandstone 1 (Miao et al. 2018), Shale (Li et al. 2021), Sandstone 2 (Chang et al. 2022), Marble (Pan et al. 2020), and Gypsum rock (Wong and Einstein 2006)) as well as 3D-printed specimens, as shown in Fig. 10b. The symbols in the figure represent experimental data, while the curves depict the results of polynomial fitting based on the experimental data. From the figure, it can be observed that when the initial flaw angles are the same, the crack initiation angles of 3D-printed gypsum specimens are slightly lower than those of natural rocks. According to the fitted curves, there is a negative correlation between the initiation angle and the flaw angle, indicating that smaller flaw angles result in larger initiation angles for the formation of new cracks. Furthermore, it is evident that the fitting curves of initiation angles with respect to flaw angles exhibit smaller discrepancies between 3D-printed rocks and sandstone. This suggests that among all the natural rocks mentioned in this study, sandstone appears to be the most promising candidate for replacement by 3D-printed gypsum specimens.

3.2.2 Volume Change of New Cracks

Quantitative analysis of the change in crack volume during uniaxial compression can aid the understanding of the failure
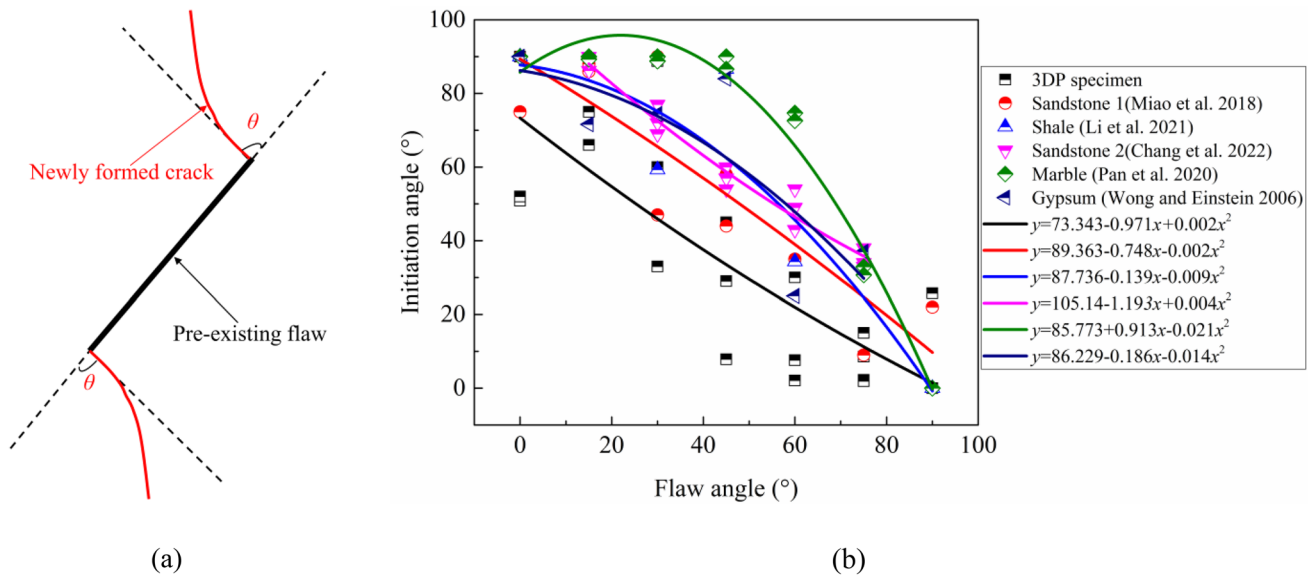
(a)   (b)

Fig. 10 Definition of initiation angle (**a**) and the relationship between initiation angle and flaw angle (**b**), where the symbols and curves represent experimental data and the results of polynomial fitting based on the experimental data, respectively

Table 2 Specifications of newly formed cracks in 3D-printed specimens containing a single flaw with different inclined angles

Crack type	Primary crack		Secondary crack		Tertiary crack	
Flaw angle	Crack pattern	Initiation angle	Crack pattern	Initiation angle	Crack pattern	Initiation angle
0°	T4	90°	M	50.87°, 52°	–	–
15°	T4	75°	S1	66°	M	33°
30°	T4	60°	S1	88.8°	M	29°
45°	T1	45°	S2	7.84°	S2	7.59°
60°	T2	30°	S2	2.09°	S2	1.89°
75°	T2, S2	15°, 8.56°	S2	2.25°	–	–
90°	T2	0°	S2	25.7°	–	–

behavior and fracture mechanisms of 3D-printed specimens. The calculation of crack volume can be expressed using Eq. 1:

$$V(X) = V_{\text{unit}} \sum_{i,j,k} I(x_i, y_j, z_k), \qquad (1)$$

where $V(X)$ is the volume of the cracks and V_{unit} represents the volume of each pixel. In this study, a resolution of 20.9 μm was used, so the volume of each pixel is equal to 9.13×10^{-6} mm^3. $\sum_{i,j,k} I(x_i, y_j, z_k)$ denotes the total number of pixels corresponding to the crack's interior. If the pixel's coordinates (x_i, y_j, z_k) are located within a crack, then $I(x_i, y_j, z_k) = 1$.

Figure 11 illustrates the change in the total crack volume and the volume of newly formed cracks as strain increases. The total crack volume refers to the combined volume of the initial flaw and the newly formed cracks.

As shown in Fig. 11a, the curve could be roughly divided into three stages: (1) The steady stage characterized by a constant total crack volume, which corresponds to the linear stage in the stress–strain curve where pore compaction is observed. (2) The slow-increase stage where the total crack volume gradually increases with strain, which corresponds to the plastic deformation stage in the stress–strain curve. (3) The rapid-increase stage where the total crack volume increases rapidly with strain, which corresponds to the post-peak stage in the stress–strain curve. The variations of the volume of newly formed cracks within the 3D-printed specimens are shown in Fig. 11b. Similar to the change of total crack volume, the volume of newly formed cracks consisted of the steady stage, slow-increase stage, and rapid-increase stage. During the steady stage, the external load on the 3D-printed specimen was relatively low, making it difficult to generate new cracks. Only some internal pores were compressed during this
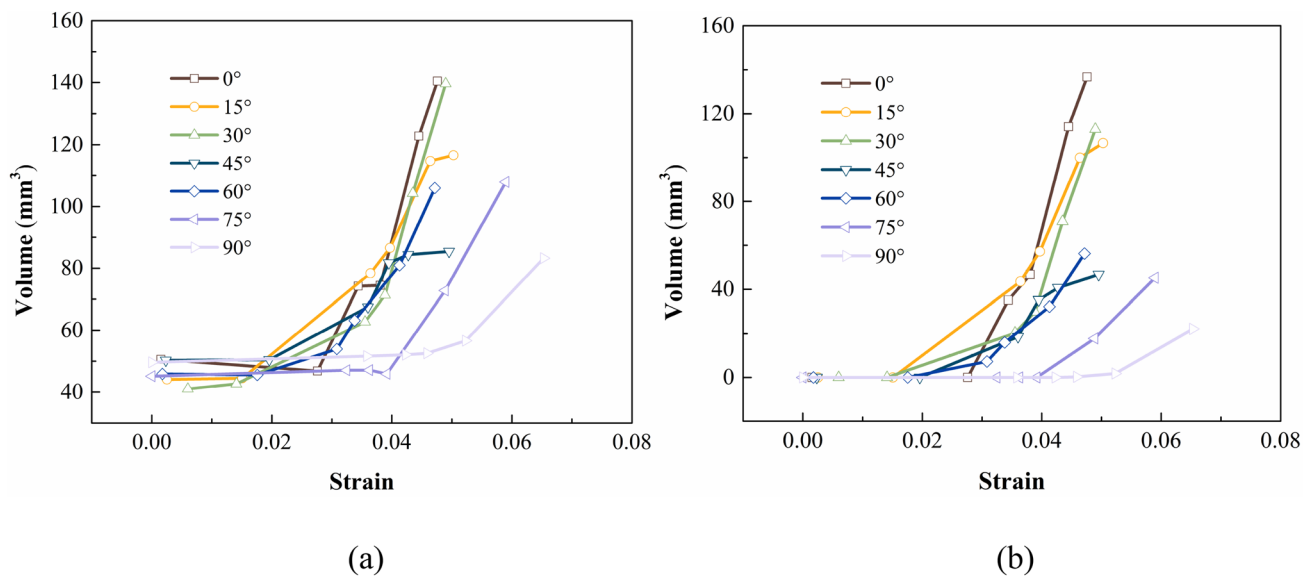
Fig. 11 Total volume of cracks versus strain (**a**) and volume of newly formed cracks versus strain (**b**)

stage, as reported in our previous research (Shao et al. 2023a, b). As the external stress applied to the 3D-printed specimen gradually increased throughout the plastic deformation stage of the stress–strain curve, micro-cracks inside the specimen gradually developed into macroscopic cracks. Since the 3D-printed sample had not failed yet, the rate of increase in crack volume was relatively slow during this stage. However, when the stress exceeded the peak strength, the 3D-printed specimen failed, and the crack volume increased sharply. Under the same strain, the 3D-printed specimens with initial crack angles between the range of $0° \leq \alpha < 45°$ exhibited significantly larger volumes of newly formed cracks compared to those with initial crack angles between $45° \leq \alpha \leq 90°$. Furthermore, the volume of newly formed cracks within the 3D-printed specimen tended to be negatively correlated with the inclined angle of the initial flaw.

3.2.3 Volume Change of the Initial Flaw

Scholars have emphasized the development of newly formed cracks in rocks under compression while simplifying initial defects as rigid bodies with constant volumes in numerical simulation studies. However, comprehending the evolution of the initial flaw is crucial for gaining valuable insights into fracture mechanics, failure behavior of rocks, and its implications for rock engineering. Figure 12 presents the evolution of the initial flaw volume observed in this study (Fig. 12a) and the normalized volume (Fig. 12b) with increasing strain. Due to the limitations of the 3D printer's printing precision and the infiltration of the binder during the

printing process, there were slight variations in the volume of the initial flaw among different 3D-printed specimens. Therefore, a normalized volume was defined by the ratio of the initial flaw volume at different strains to the initial flaw volume at no load. The derivation is expressed by Eq. 2:

$$V_{\text{Normalized}} = \frac{V_1}{V_0}, \tag{2}$$

where $V_{\text{Normalized}}$ is the normalized volume. V_1 represents the flaw volume at different strain levels and V_0 denotes the initial flaw volume before loading.

The volume of the initial crack showed different trends for different crack angles. Specifically, for flaw angles in the range of $0° \leq \alpha \leq 45°$, the flaw volume gradually decreased with increasing strain. Conversely, for flaw angles in the range of $45° < \alpha \leq 90°$, the flaw volume illustrated the opposite trend. This behavior could be explained through the crack evolution processes shown in Figs. 8 and 9. The initial flaw with angles between 0° and 45°, primarily experienced compressive stress, leading to volume reduction. Conversely, the initial flaw with angles between 45° and 90°, mainly experienced shear or tensile stress, resulting in volume expansion.

3.3 Damage Evolution

3.3.1 Damage Evolution in 3D

In rock mechanics, the damage variable has been used to describe the damage behavior and evolution of rocks under

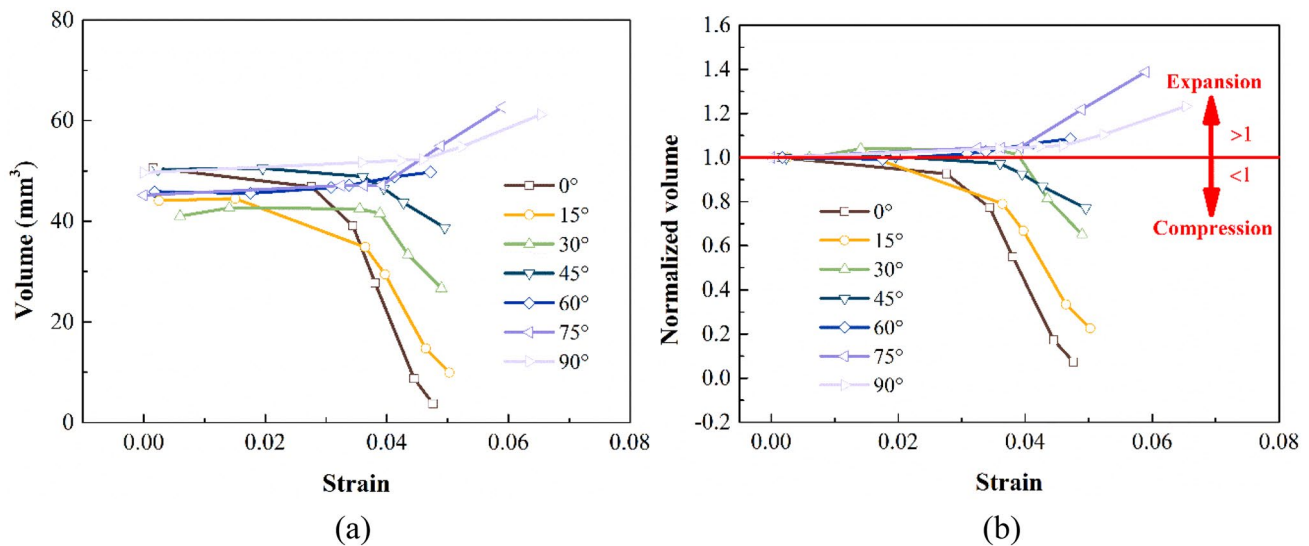**Fig. 12** Volume of initial flaw versus strain (**a**) and normalized volume of initial flaw versus strain (**b**)

loading, as a quantitative description of the internal microstructure and macroscopic performance of rocks (Liu and Zhao 2021). Based on the grayscale data from CT images, the damage variable can be defined as the ratio of the damaged area to the total area of the tested sample, as reported in the literature (Sun et al. 2020; Zexun et al. 2011; Zhong et al. 2019). The damage variable can be expressed as the ratio of the crack volume to the total volume of the tested sample in 3D, as shown in Eq. 3.

$$D_{3d} = \frac{V_{cracks}}{V_{total}}, \tag{3}$$

where D_{3d} represents the damage value in 3D. V_{cracks} is the volume of cracks. V_{total} denotes the total volume of the tested object.

Figure 13 illustrates the evolution of damage values with respect to strain, calculated by Eq. 3. By comparing Figs. 11, 12, and 13, it was observed that the damage evolution in the 3D-printed specimens was generally consistent with the variation of crack volumes. Both the total damage and the damage solely considering the newly formed cracks, represented by Fig. 13a and b, respectively, could be roughly divided into three stages: (1) Early compression stage: In this stage, no new cracks were generated and the damage variable remained nearly constant. (2) Damage initiation and development stage: Micro-cracks within the 3D-printed sample started to initiate and develop, forming a significant region of plastic deformation that absorbed stress and underwent continuous plastic deformation. As shown in Fig. 9, tensile cracks were predominantly formed during this phase. (3) Damage failure stage: This stage corresponds to the post-peak failure phase of the stress–strain curve of

the 3D-printed specimen. During this stage, tensile cracks within the 3D-printed specimen continued to develop as the strain increased, accompanied by the initiation and development of shear cracks. As a result, the rate of increase in the damage variable within the specimen was much higher during the damage failure stage compared to the previous stages. Figure 13c illustrates the change in damage values attributed to the initial flaw as the loading strain increases. These values are derived by subtracting the damage values associated with newly formed cracks (as depicted in Fig. 13b) from the total damage within the 3D-printed specimens (as shown in Fig. 13a). Regarding the damage evolution of the initial flaw, for initial flaw angles of $0° \leq \alpha \leq 45°$, the damage variable gradually increased with strain. Conversely, for initial flaw angles of $45° < \alpha \leq 90°$, the damage variable decreased with strain.

3.3.2 Damage Evolution in 2D

Although the 3D damage value can effectively capture the internal damage evolution of the 3D-printed specimen, it represents a global value that cannot reflect the spatial distribution of damage; The distribution of damage within a specimen is non-uniform due to strain concentration and stress concentration. To investigate the damage distribution, researchers (Baines et al. 2007; Duan et al. 2022) have assessed the internal damage distribution by computing the 2D damage variable using Eq. 4:

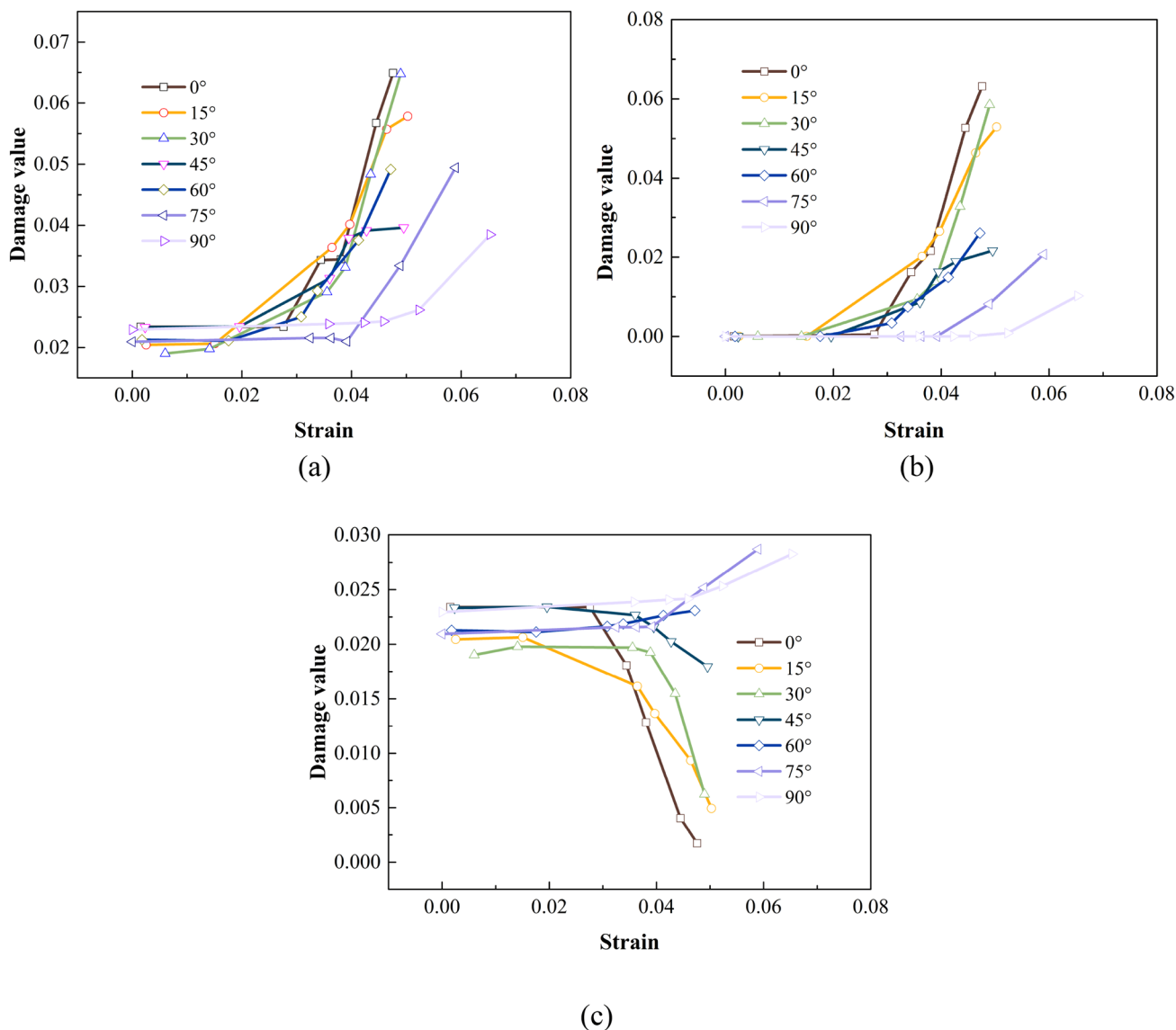$$D_{2d} = \frac{A_{cracks}}{A_{total}}, \tag{4}$$

Fig. 13 Total damage evolution (**a**), damage evolution only considering the newly formed cracks (**b**), and damage evolution of the initial flaw (**c**) with respect to strain

where D_{2d} represents the damage value in 2D. A_{cracks} is the area of cracks, and A_{total} denotes the total area of the tested object.

Figure 14 presents the 2D damage value of the initial flaw at different elevations and strains. The bottom of the analyzed region, shown in Fig. 6c, was considered to be elevation of 0. The results showed that the inclination angle of the initial flaw significantly influenced the damage evolution. Specifically, when the inclination angle was within the range of $0° \leq \alpha \leq 45°$, the damage value of the initial flaw decreased with increasing strain at the same elevation. After specimen failure, the flaw underwent

compaction compared to its initial state. On the other hand, when the angle was within the range of $45° < \alpha \leq 90°$, the damage value increased with increasing strain at the same elevation, and after failure, the flaw was more expansive compared to its initial state. This phenomenon can be mainly attributed to the non-uniform stress distribution and the type of newly formed cracks within the 3D-printed specimens. To the best of our knowledge, this is the first study to report the initial crack's damage evolution in 3D-printed specimens. These findings can provide valuable insights into the damage patterns of natural rock
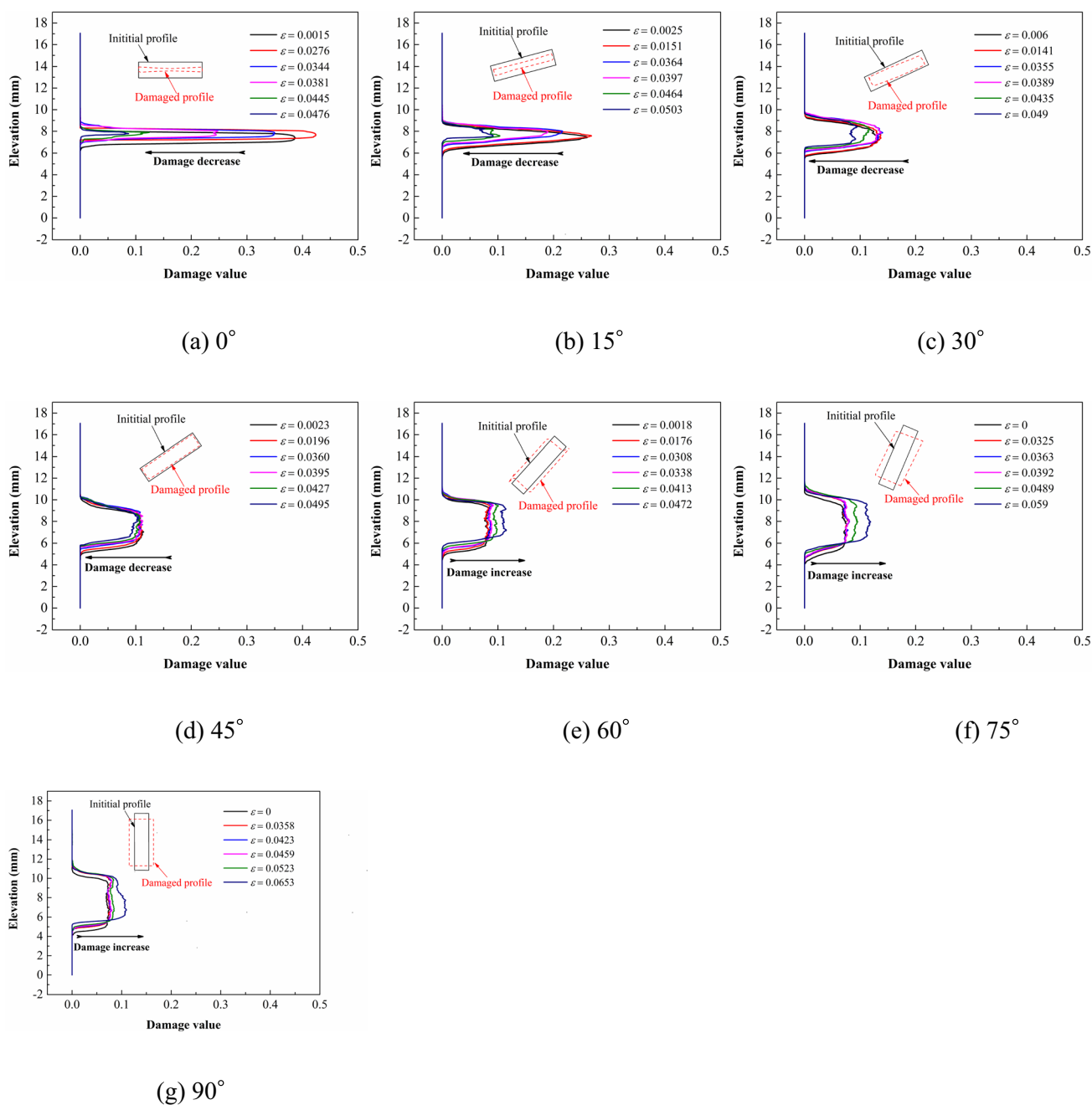
(a) 0°

(b) 15°

(c) 30°

(d) 45°

(e) 60°

(f) 75°

(g) 90°

Fig. 14 Damage value of the initial flaw at different scanning steps versus elevations. The black rectangles represent the initial morphology of the initial flaw, while the red dashed boxes indicate the morphology after specimen failure

with initial flaws, and thereby enhance our understanding of the fracture mechanics and failure behavior of rocks.

Figure 15 depicts the damage caused by newly formed cracks at different elevations and strains. During the compression of 3D-printed specimens, damage typically emanated from the vicinity of the initial flaw and gradually propagated towards the ends of the specimen, exhibiting a noticeable symmetry with respect to the center of the initial flaw. The magnitude of damage was smaller for specimens

with initial flaws of larger inclination angles. Specifically, under identical strain conditions, specimens with an inclination angle of $\alpha = 0°$ exhibited the most substantial post-failure damage, while specimens with an inclination angle of $\alpha = 90°$ displayed the least damage. Furthermore, the damage evolution curves considering the newly formed cracks within the specimens with initial flaws inclined between $0° \leq \alpha \leq 45°$ exhibited a more pronounced pattern compared to those with initial flaws inclined between

(a) 0°

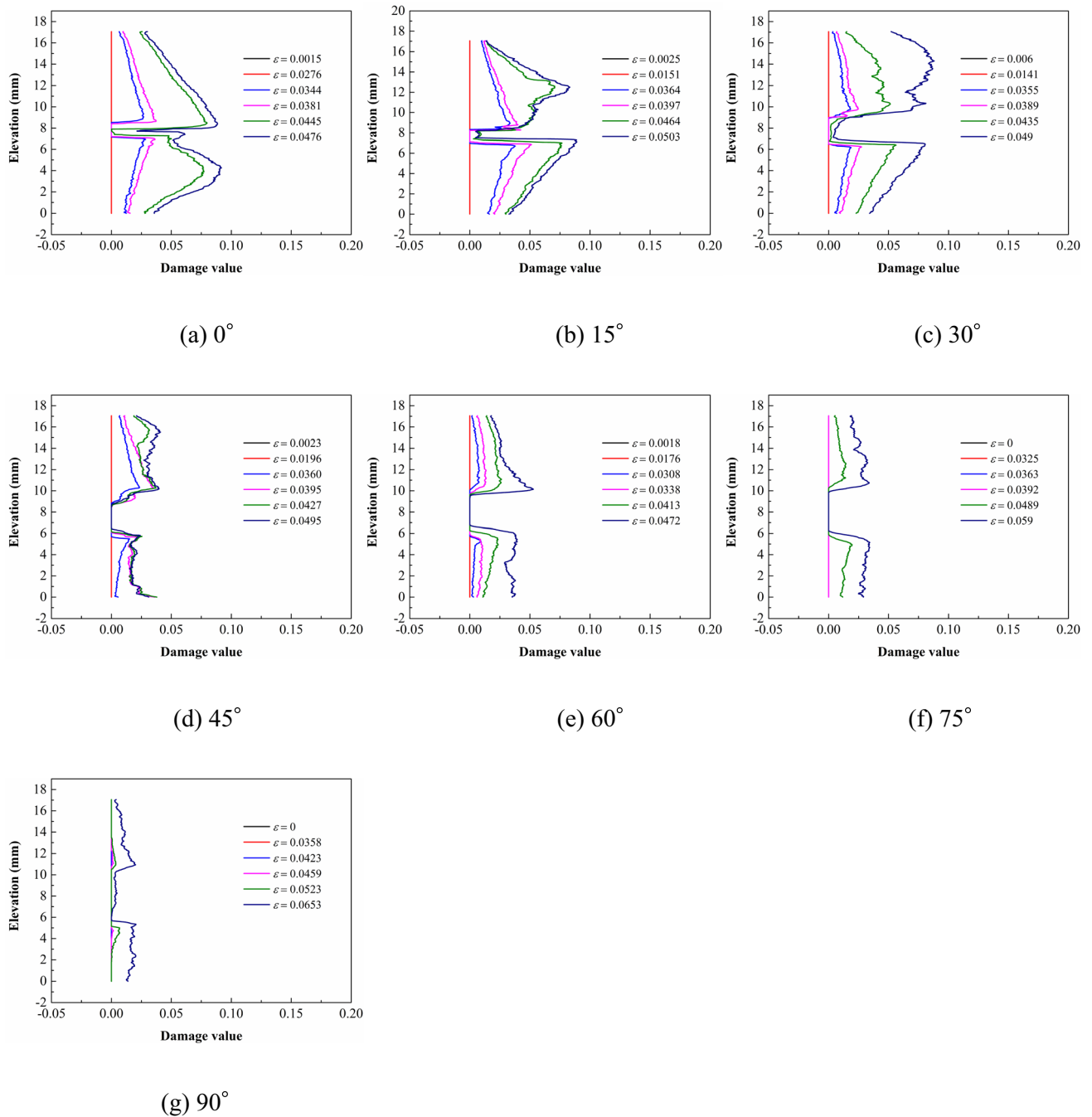(b) 15°

(c) 30°

(d) 45°

(e) 60°

(f) 75°

(g) 90°

Fig. 15 Damage value considering the newly formed cracks at different scanning steps versus elevations

$45° < \alpha \leq 90°$. This distinction can be primarily attributed to the number of newly formed cracks within the 3D printed specimens and the extent of crack propagation, as illustrated in Fig. 9.

3.4 Comparison of Failure Modes Between 3D-Printed Specimens and Natural Rocks

The surface crack patterns observed after the failure of the 3D-printed gypsum specimens were compared with those of 3D-printed sand specimens reported by Yu et al. (2021), and natural rock samples reported by Miao et al. (2018). The crack patterns are presented and compared in Fig. 16. When the inclination angle of the initial flaw was 0°, 15°,
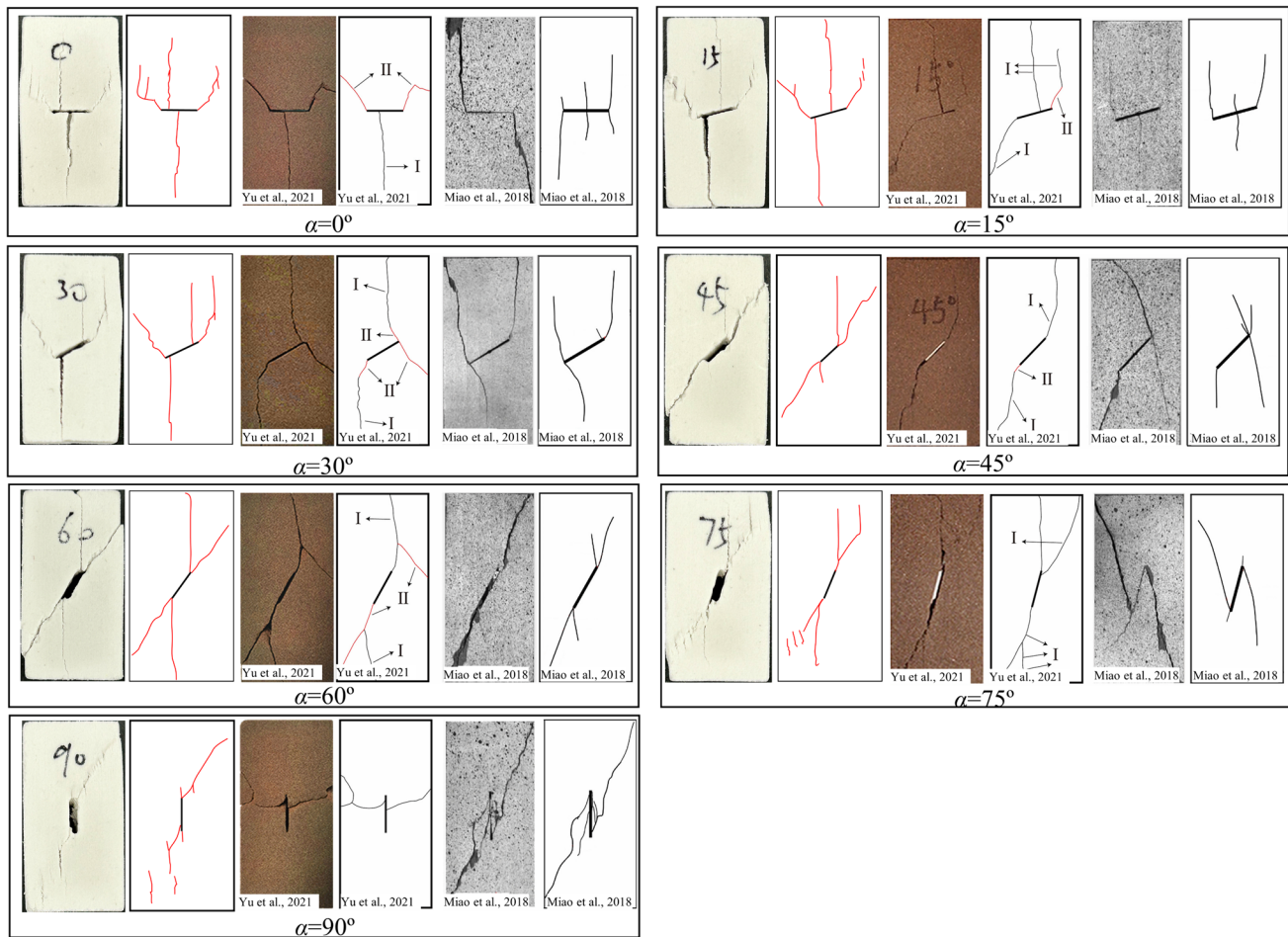
Fig. 16 Comparison of crack patterns between 3D-printed gypsum specimens, 3D-printed sand specimens, and natural rocks

and 30°, shear cracks appeared at the flaw tips and tensile cracks formed in the middle of the flaw of natural rocks and 3D-printed gypsum specimens. These crack behaviors were consistent between 3D-printed gypsum specimens and natural rocks, but those of 3D-printed sand specimens were significantly different. At an inclination angle of 45° and 60°, both shear and tensile cracks occurred at the flaw tips of natural rocks and 3D-printed gypsum specimens, with similar crack propagation directions. Although shear and tensile cracks were also identified in the 3D-printed sand specimens, the angles of crack initiation and crack propagation differed significantly from those observed in natural rock. Notably, at an inclination angle of 75°, the crack behaviors in 3D-printed gypsum specimens and 3D-printed sand specimens were similar, but both differed substantially from the failure mode of natural rock. At an inclination angle of 90°, failure in natural rock and 3D-printed gypsum specimens resulted from inclined shear cracks, while in 3D-printed sand specimens, failure occurred due to horizontal shear cracks.

To compare the crack patterns in terms of failure modes, the failure modes of the crack patterns in Fig. 16

were categorized into tensile failure, shear failure, and tensile-shear compound failure, following the classification method proposed by Zhu et al. (2016). The classified failure modes are tabulated in Table 3. The results showed that the tensile-shear composite failure mode was the major failure mode in 3D-printed gypsum specimens, 3D-printed sand specimens, and natural rock when the inclination angle was in the range of 0°–60°. However, at an inclination angle of 75°, the failure mode of natural rock was shear failure, while 3D-printed gypsum specimens and 3D-printed sand specimens exhibited tensile-shear composite failure and tensile failure, respectively. When the inclination angle was 90°, 3D-printed gypsum specimens and natural rock showed shear failure, while 3D-printed sand specimens denoted the tensile-shear composite failure.

Table 3 Comparison of failure modes between 3D-printed gypsum specimens, 3D-printed sand specimens, and natural rocks

Failure modes		Tensile failure	Shear failure	Tensile-shear compound failure
3D-printed gypsum specimens	0°			★
	15°			★
	30°			★
	45°			★
	60°			★
	75°			★
	90°		★	
3D-printed sand specimens	0°			★
	15°			★
	30°			★
	45°			★
	60°			★
	75°	★		
	90°			★
Natural rocks	0°			★
	15°			★
	30°			★
	45°			★
	60°			★
	75°		★	
	90°		★	

4 Conclusion

This study conducted a comprehensive analysis of crack behavior in 3D-printed rock-like specimens with a single flaw using in-situ Micro-CT imaging during compression testing. Seven specimens with varying flaw angles were examined. Utilizing the acquired 2D CT images and 3D reconstruction, crack patterns and key parameters such as initiation angles, volume changes of cracks, and damage evolution were visually and quantitatively analyzed to characterize the crack behavior of 3D-printed specimens during in-situ uniaxial compression testing. Key findings include:

1. Tensile cracks initiate first, followed by shear or mixed cracks at flaw tips. Shear cracks become predominant as the flaw angle increases, with crack propagation opposing the flaw angle.
2. Flaw volume and damage decrease with increasing axial strain for angles between 0° and 45°, but increase for angles between 45° and 90°.
3. Volume of newly formed cracks changes exhibit three stages with strain: steady, slow increase, and rapid increase.
4. Comparison with natural rocks indicates similar failure modes and crack patterns, suggesting the potential of 3D printing for studying rock fracture behavior.

The utilization of 3D-printed gypsum specimens in this study, characterized by relatively low strength, restricts their compatibility with rocks with similar lower strength properties, such as sandstone. Consequently, the generalizability and applicability of the findings are constrained by this limitation.

Declarations

References

Aliabadian Z, Sharafisafa M, Tahmasebinia F, Shen L (2021) Experimental and numerical investigations on crack development in 3D printed rock-like specimens with pre-existing flaws. Eng Fract Mech 241:107396

Baines T, Lightfoot H, Steve E, Neely A, Greenough R, Peppard J, Roy R, Shehab E, Braganza A, Tiwari A (2007) Proceedings of the institution of mechanical engineers. J Eng Manuf 221:1543–1552

Ban Y, Xie Q, Duan J, Fu X (2022) Influences of inclined pre-existing flaw on shale failure modes in uniaxial compression tests. Minerals 12:1330

Cao P, Liu T, Pu C, Lin H (2015) Crack propagation and coalescence of brittle rock-like specimens with pre-existing cracks in compression. Eng Geol 187:113–121

Chang X, Zhang X, Dang FN, Zhang BF, Chang FQ (2022) Failure behavior of sandstone specimens containing a single flaw under true triaxial compression. Rock Mech Rock Eng 55:2111–2127

Dewanckele J, Boone M, De Kock T, De Boever W, Brabant L, Boone M, Fronteau G, Dils J, Van Hoorebeke L, Jacobs P (2013) Holistic approach of pre-existing flaws on the decay of two limestones. Sci Total Environ 447:403–414

Duan Y, Feng X-T, Li X, Yang B (2022) Mesoscopic damage mechanism and a constitutive model of shale using in-situ X-ray CT device. Eng Fract Mech 269:108576

Dyskin A, Germanovich L, Jewell R, Joer H, Krasinski J, Lee K, Roegiers J, Sahouryeh E, Ustinov K (1994) Study of 3-d mechanisms of crack growth and interaction in uniaxial compression. ISRM News J 2(17–20):22–24

Dyskin A, Sahouryeh E, Jewell R, Joer H, Ustinov K (2003) Influence of shape and locations of initial 3-D cracks on their growth in uniaxial compression. Eng Fract Mech 70:2115–2136

Feng X-T, Ding W, Zhang D (2009) Multi-crack interaction in limestone subject to stress and flow of chemical solutions. Int J Rock Mech Min 46:159–171

Feng X-T, Gong Y-H, Zhou Y-Y, Li Z-W, Liu X-F (2019) The 3D-printing technology of geological models using rock-like materials. Rock Mech Rock Eng 52:2261–2277

Fereshtenejad S, Song J-J (2016) Fundamental study on applicability of powder-based 3D printer for physical modeling in rock mechanics. Rock Mech Rock Eng 49:2065–2074

Gao Y-T, Wu T-H, Zhou Y (2021) Application and prospective of 3D printing in rock mechanics: A review. Int J Miner Metall Mater 28:1–17

He L, Xiao H, Cui Y, Liu S, Chen J (2021) Review of visualisation methods of studying the seepage mechanism in fractured rocks. Geomech Geophys Geo-Energy Geo-Resour 7:1–25

Ishutov S, Hasiuk FJ, Harding C, Gray JN (2015) 3D printing sandstone porosity models. Interpretation 3:SX49–SX61

Ishutov S, Hasiuk FJ, Fullmer SM, Buono AS, Gray JN, Harding C (2017) Resurrection of a reservoir sandstone from tomographic data using three-dimensional printing. AAPG Bull 101:1425–1443

Ishutov S, Hodder K, Chalaturnyk R, Zambrano-Narvaez G (2021) Replication of carbonate reservoir pores at the original size using 3D printing. Petrophysics 62:477–485

Jiang C, Zhao G-F (2015) A preliminary study of 3D printing on rock mechanics. Rock Mech Rock Eng 48:1041–1050

Jiang C, Zhao G-F, Zhu J, Zhao Y-X, Shen L (2016a) Investigation of dynamic crack coalescence using a gypsum-like 3D printing material. Rock Mech Rock Eng 49:3983–3998

Jiang Q, Feng X, Song L, Gong Y, Zheng H, Cui J (2016b) Modeling rock specimens through 3D printing: Tentative experiments and prospects. Acta Mech Sin 32:101–111

Kang G, Han Y, Xi X, Li L, Yang S, Zhu L, Liu M, Tan S, Yan B (2022) An improved scattering correction method for model analysis of cone-beam CT. In: 2022 2nd International conference on bioinformatics and intelligent computing

Kong L, Ostadhassan M, Li C, Tamimi N (2018) Pore characterization of 3D-printed gypsum rocks: a comprehensive approach. J Mater Sci 53:5063–5078

Li Y-P, Chen L-Z, Wang Y-H (2005) Experimental research on pre-cracked marble under compression. Int J Solids Struct 42:2505–2516

Li L, Liu Y, Liu W, Zhang X, Chen J, Jiang D, Fan J (2021) Crack evolution and failure modes of shale containing a pre-existing fissure under compression. ACS Omega 6:25461–25475

Liang Z, Xing H, Wang S, Williams D, Tang C (2012) A three-dimensional numerical investigation of the fracture of rock specimens containing a pre-existing surface flaw. Comput Geotech 45:19–33

Liu K, Zhao J (2021) Progressive damage behaviours of triaxially confined rocks under multiple dynamic loads. Rock Mech Rock Eng 54:3327–3358

Liu H, Meng F, Hua S (2021) 4d mapping of the fracture evolution in a printed gypsum-like core by using x-ray ct scanning. Adv Civ Eng 2021:1–12

Mandal S, Basu B (2018) Probing the influence of post-processing on microstructure and in situ compression failure with in silico modeling of 3D-printed scaffolds. J Mater Res 33:2062–2076

Mei S, Feng X-T, Li Z, Yang C, Gao J (2022) A novel 3D printing technology for synthetic hard rock and the fabrication of Jinping marble. Rock Mech Rock Eng 55:7695–7714

Miao S, Pan P-Z, Wu Z, Li S, Zhao S (2018) Fracture analysis of sandstone with a single filled flaw under uniaxial compression. Eng Fract Mech 204:319–343

Niu Q, Jiang L, Li C, Zhao Y, Wang Q, Yuan A (2023) Application and prospects of 3d printing in physical experiments of rock mass mechanics and engineering: materials, methodologies and models. Int J Coal Sci Technol 10:5

Pan PZ, Miao ST, Jiang Q, Wu ZH, Shao CY (2020) The influence of infilling conditions on flaw surface relative displacement induced cracking behavior in hard rock. Rock Mech Rock Eng 53:4449–4470

Pardoen B, Bésuelle P, Dal Pont S, Cosenza P, Desrues J (2020) Accounting for small-scale heterogeneity and variability of clay rock in homogenised numerical micromechanical response and microcracking. Rock Mech Rock Eng 53:2727–2746

Schultz RA (2019) Geologic fracture mechanics. Cambridge University Press, Cambridge

Shao Y, Kim J, Song J-J (2023a) 4D imaging of crack evolution and failure mode in 3DP rock-like samples under uniaxial compression by using in-situ Micro-CT technology. In: 15th ISRM congress 2

Shao Y, Yang J, Kim J, Song J-J, Moon J, Han J (2023b) A comprehensive experimental study on mechanical anisotropy and failure mode of 3D printed gypsum rocks: from composition and microstructure to macroscopic mechanical properties response. Rock Mech Rock Eng 56:6503–6528

Sharafisafa M, Shen L, Xu Q (2018) Characterisation of mechanical behaviour of 3D printed rock-like material with digital image correlation. Int J Rock Mech Min 112:122–138

Song R, Liu J, Yang C, Sun S (2022) Study on the multiphase heat and mass transfer mechanism in the dissociation of methane hydrate in reconstructed real-shape porous sediments. Energy 254:124421

Song R, Tian J, Wu M, Liu J (2023a) Experimental and numerical modeling of deformation-cracking mechanics of 3D-printed rock samples with single fracture. Adv Geo-Energy Res 8:126–135

Song R, Wu M, Wang Y, Liu J, Yang C (2023b) In-situ X-CT scanning and numerical modeling on the mechanical behavior of the 3D printing rock. Powder Technol 416:118240

Sun X, Li X, Zheng B, He J, Mao T (2020) Study on the progressive fracturing in soil and rock mixture under uniaxial compression conditions by CT scanning. Eng Geol 279:105884

Tian W, Han N (2017) Mechanical properties of rock specimens containing pre-existing flaws with 3 D printed materials. Strain 53:e12240

Tutluoğlu L, Öge İF, Karpuz C (2015) Relationship between pre-failure and post-failure mechanical properties of rock material of different origin. Rock Mech Rock Eng 48:121–141

Wang D-J, Tang H, Elsworth D, Wang C (2019) Fracture evolution in artificial bedded rocks containing a structural flaw under uniaxial compression. Eng Geol 250:130–141

Wang Y, Deng H, Deng Y, Chen K, He J (2021) Study on crack dynamic evolution and damage-fracture mechanism of rock with pre-existing cracks based on acoustic emission location. J Petrol Sci Eng 201:108420

Wong L, Einstein H (2009) Systematic evaluation of cracking behavior in specimens containing single flaws under uniaxial compression. Int J Rock Mech Min 46:239–249

Wong R, Chau KT, Tang C, Lin P (2001) Analysis of crack coalescence in rock-like materials containing three flaws—part I: experimental approach. Int J Rock Mech Min 38:909–924

Wong LN, Einstein H. (2006). Fracturing behavior of prismatic specimens containing single flaws. In: ARMA US rock mechanics/geomechanics symposium

Wu Z, Zhang B, Weng L, Liu Q, Wong LNY (2020) A new way to replicate the highly stressed soft rock: 3D printing exploration. Rock Mech Rock Eng 53:467–476

Wu H, Ju Y, Han X, Ren Z, Sun Y, Zhang Y, Han T (2022) Size effects in the uniaxial compressive properties of 3D printed models of rocks: an experimental investigation. Int J Coal Sci Technol 9:83

Xu L, Gong F, Luo S (2021a) Effects of pre-existing single crack angle on mechanical behaviors and energy storage characteristics of red sandstone under uniaxial compression. Theoret Appl Fract Mech 113:102933

Xu Q, Jiang L, Ma C, Niu Q, Wang X (2021b) Effect of layer thickness on the physical and mechanical properties of sand powder 3D printing specimens. Front Earth Sci 9:763202

Yang S-Q, Huang Y-H (2017) An experimental study on deformation and failure mechanical behavior of granite containing a single fissure under different confining pressures. Environ Earth Sci 76:1–22

Yang S-Q, Liu X-R, Jing H-W (2013) Experimental investigation on fracture coalescence behavior of red sandstone containing two unparallel fissures under uniaxial compression. Int J Rock Mech Min 63:82–92

Yang S-Q, Huang Y-H, Tian W-L, Zhu J-B (2017) An experimental investigation on strength, deformation and crack evolution behavior of sandstone containing two oval flaws under uniaxial compression. Eng Geol 217:35–48

Yin P, Wong R, Chau KT (2014) Coalescence of two parallel pre-existing surface cracks in granite. Int J Rock Mech Min 68:66–84

Yin P, Zhao C, Ma J, Yan C, Huang L (2020) Experimental study of non-linear fluid flow though rough fracture based on fractal theory and 3D printing technique. Int J Rock Mech Min 129:104293

Yu C, Tian W, Zhang C, Chai S, Cheng X, Wang X (2021) Temperature-dependent mechanical properties and crack propagation modes of 3D printed sandstones. Int J Rock Mech Min 146:104868

Zexun Y, Lingtao M, Dan Z, Zhenyu C (2011) Soft soil microstructure character analysis with CT. Appl Mech Mater. https://doi.org/10.4028/www.scientific.net/AMM.90-93.588

Zhong J, Wang Z, Wang L, Zhao J, Ren W, Zhou H (2019) Characteristics of damage evolution of deep coal based on CT three-dimensional reconstruction. J China Coal Soc 44:1482–1494

Zhou T, Zhu J (2018) Identification of a suitable 3D printing material for mimicking brittle and hard rocks and its brittleness enhancements. Rock Mech Rock Eng 51:765–777

Zhou X, Bi J, Qian Q (2015) Numerical simulation of crack growth and coalescence in rock-like materials containing multiple pre-existing flaws. Rock Mech Rock Eng 48:1097–1114

Zhou T, Zhu J, Ju Y, Xie H (2019) Volumetric fracturing behavior of 3D printed artificial rocks containing single and double 3D internal flaws under static uniaxial compression. Eng Fract Mech 205:190–204

Zhou T, Zhu J, Xie H (2020) Mechanical and volumetric fracturing behaviour of three-dimensional printing rock-like samples under dynamic loading. Rock Mech Rock Eng 53:2855–2864

Zhou XP, Zhang JZ, Yang SQ, Berto F (2021) Compression-induced crack initiation and growth in flawed rocks: a review. Fatigue Fract Eng Mater Struct 44:1681–1707

Zhu T, Jing H, Su H, Yin Q, Du M, Han G (2016) Physical and mechanical properties of sandstone containing a single fissure after exposure to high temperatures. Int J Min Sci Technol 26:319–325

Zhu J, Zhou T, Liao Z, Sun L, Li X, Chen R (2018) Replication of internal defects and investigation of mechanical and fracture behaviour of rock using 3D printing and 3D numerical methods in combination with X-ray computerized tomography. Int J Rock Mech Min 106:198–212

Zou C, Wong LNY (2014) Experimental studies on cracking processes and failure in marble under dynamic loading. Eng Geol 173:19–31